




Structural, optical and giant dielectric constant properties of pure ktenasite and schulenbergite/CuO minerals

S. M. Yakout^{1,*} , A. M. Youssef¹, and Sahar M. Mousa¹

¹Inorganic Chemistry Department, National Research Centre (NRC), El Buhouth St., Dokki, Cairo 12622, Egypt

Received: 7 March 2023

Accepted: 10 May 2023

Published online:
29 May 2023

© The Author(s) 2023

ABSTRACT

In this study, schulenbergite [(Cu,Zn)₇(SO₄)₂(OH)₁₀·3H₂O]/CuO and pure ktenasite [(Cu,Zn)₅(SO₄)₂(OH)₆·6H₂O] minerals were simply synthesized via addition of sodium sulfide (Na₂S) to a mixture of nanosized CuO powder dispersed into Zn(NO₃)₂·6H₂O solution. The X-ray diffraction patterns illustrate the formation of schulenbergite/CuO mineral with ratio of 69:31% and 87/13% owing to additions of 0.1 and 0.2 mol L⁻¹ Na₂S, respectively. The addition of 0.4 mol L⁻¹ Na₂S substance lead to formation of pure ktenasite [(Cu,Zn)₅(SO₄)₂(OH)₆·6H₂O] mineral. The absorption vibration modes based on Fourier-transform infrared (FTIR) analysis verified the formation of schulenbergite/CuO and pure ktenasite compositions. The scanning electron microscope micrographs of schulenbergite/CuO and pure ktenasite samples reveal the formation of mixed grains with needle, sheets, cotton and wool shapes. The selected area electron diffraction images of the synthesized powders show strong dot-rings, indicating polycrystalline nature. Optically, all samples possess a high absorption ability for infrared-visible light wavelengths. At lower frequencies, the pellet of pure ktenasite sample exhibits giant dielectric constant characteristics. Exactly, pure ktenasite sample reveals a dielectric constant value of $\sim 1.3 \times 10^6$ at frequency of 42 Hz. For schulenbergite/CuO (87/13%) sample, a large dielectric constant value of ~ 5311 was measured at frequency of 42 Hz. The colossal and variable relative permittivity values make the pure ktenasite [(Cu,Zn)₅(SO₄)₂(OH)₆·6H₂O] mineral is a suggested material for energy storage applications.

Address correspondence to E-mail: s_mabrok2002@yahoo.com

1 Introduction

Design and synthesis of new materials and compositions can help in solving of many problems in different fields including biological, medical, environmental, magnetic targeting and separators, and energy storage applications [1–8]. Besides, the explore of the unique features and functions of the materials increases the knowledge of the characteristics of the material world in natural sciences and leads to various industrial and technological applications [9–14]. Discovering of nanomaterials with advanced optical and morphological properties have a great benefit in the photodegradation of industrial organic pollutants which discharge into water resources [15–21]. On the other hand, nanocomposites such as $\text{DyMn}_2\text{O}_5/\text{Ba}_3\text{Mn}_2\text{O}_8$ were synthesized via the hydrothermal technique as potential hydrogen storage materials [22]. In the same context, study of colossal relative permittivity (dielectric constant) compositions is very important for technological and capacitive energy storage applications [23–25]. The colossal permittivity structures can be defined as the materials that have relative permittivity (ϵ_r) value usually greater than 10^3 and also reveal extreme polarization in an applied electric field [26]. These materials have promising applications in electronic, multilayer ceramic capacitors, memory and energy storage devices [26]. The colossal dielectric constant characteristics have been reported for numerous metal oxides and perovskites structures [26–28]. With respect to mineral materials, Zheng et al. studied the dielectric characteristics of the hard rock minerals (Calcite, Diopside, Albite, Hornblende or Olivine) and implications for microwave-assisted rock fracturing [29]. Very rare studies have been carried out on the preparation and characterization of new copper–zinc (Cu,Zn) sulfate minerals such as hodge-smithite $[(\text{Cu,Zn})_6\text{Zn}(\text{SO}_4)_2(\text{OH})_{10}\cdot 3\text{H}_2\text{O}]$, belogubite $[\text{CuZn}(\text{SO}_4)_2\cdot 10\text{H}_2\text{O}]$ schulenbergite $[(\text{Cu,Zn})_7(\text{SO}_4)_2(\text{OH})_{10}\cdot 3\text{H}_2\text{O}]$ and ktenasite $[(\text{Cu,Zn})_5(\text{SO}_4)_2(\text{OH})_6\cdot 6\text{H}_2\text{O}]$ [30–35]. Besides that, the optical, electrical and dielectric characteristics of these minerals are not studied until now. In Germany, schulenbergite was first described in 1984 by Hoderberg et al. [31]. With respect to ktenasite mineral as a basic copper zinc sulfate, it was first reported by Kokkoros in 1950 (Greece) [32]. Only, in 2004, Mei et al. reported the synthesis of pure ktenasite mineral

using ZnO powder with CuSO_4 solution at room temperature [32]. According to our knowledge, there is no detailed results in the published literature about the optical, ac electrical conductivity and dielectric characteristics of schulenbergite and pure ktenasite minerals were found. In this study, we reported a new room temperature synthesis route based on coprecipitation method for schulenbergite and pure ktenasite minerals using nanosized CuO powder– $\text{Zn}(\text{NO}_3)_2\cdot 6\text{H}_2\text{O}$ solution and sodium sulfide (Na_2S) substance. The structural, morphological and optical properties of the synthesized schulenbergite and pure ktenasite minerals were investigated by using X-ray diffraction (XRD), Fourier-transform infrared spectroscopy (FTIR), scanning electron microscope (SEM), transmission electron microscope (TEM) and diffuse reflectance techniques. Additionally, the ac electrical conductivity and dielectric characteristics of the fabricated schulenbergite and ktenasite pellets were measured and discussed. Remarkably, the pellet of the pure ktenasite powder has shown giant dielectric constant (relative permittivity) characteristics with a dielectric constant value of $\sim 1.3 \times 10^6$ at frequency of 42 Hz. The giant relative permittivity values make the pure ktenasite $[(\text{Cu,Zn})_5(\text{SO}_4)_2(\text{OH})_6\cdot 6\text{H}_2\text{O}]$ mineral is a promising material for energy storage applications.

2 Experimental

2.1 Synthesis of CuO nanopowder

CuO nanoparticles was synthesized through using the coprecipitation method. Such method is a simple way which attracts significant interest in industries owing to low energy and temperature, inexpensive and cost-effective approach for a large scale production. Exactly, 10 g of copper nitrate trihydrate $[\text{Cu}(\text{NO}_3)_2\cdot 3\text{H}_2\text{O}]$ was dissolved in 100 mL deionized water ($\text{D-H}_2\text{O}$). Then, 0.1 M of sodium hydroxide (NaOH) was gradually dropped until the pH reached 12 at temperature of 50 °C under continuous stirring (400 rpm) for 1 h. The obtained precipitate stands still for 24 h until it changed from blue to black color. The black precipitate was washed by deionized water several times while waiting for pH to reach 7 then dried at 100 °C for 5 h.

2.2 Synthesis of schulenbergite [(Cu,Zn)₇(SO₄)₂(OH)₁₀·3H₂O]/CuO minerals

Schulenbergit/CuO mineral with ratios (69:31%) and (87/13%) were produced by the addition of 0.1 and 0.2 mol L⁻¹ Na₂S substance to mixture of nano-sized CuO powder dispersed into Zn(NO₃)₂·6H₂O solution, respectively. Typically, 1.2 g of the synthesized pure CuO nanoparticles was mixed with 200 mL isopropanol and sonicated for 15 min with adjusting the pH to 10 by addition of NH₄OH. Then, 0.2 M Zn(NO₃)₂·6H₂O was added to the above solution with continuous stirring for 1 h. Finally, 0.1 and 0.2 mol L⁻¹ Na₂S substance was added to the prepared CuO-Zn(NO₃)₂·6H₂O mixture with stirring for 2 h and then aged for 3 days. The obtained product was washed with deionized water for many times (decantation) and then dried at 70 °C.

2.3 Synthesis of pure ktenasite [(Cu,Zn)₅(SO₄)₂(OH)₆·6H₂O] mineral

For pure ktenasite mineral, 1.2 g of the synthesized CuO nanoparticles was mixed with 200 mL isopropanol and sonicated for 15 min with regulating the pH to 10 through addition of NH₄OH solution. Then, 0.2 M Zn(NO₃)₂·6H₂O was added to the above solution with continuous stirring for 1 h. After that, 0.4 mol L⁻¹ Na₂S substance was added to the above mixture with stirring for 2 h and then aged for 3 days.

The obtained results illustrated that the concentration of Na₂S substance plays an important role in the ratio of the schulenbergit/CuO mineral formed or also the formation of pure ktenasite mineral.

2.4 Characterization and measurements

The X-ray diffraction (XRD) measurements for the synthesized Schulenbergit/CuO pure ktenasite were performed by using PANalytical X-ray diffraction equipment model X'Pert PRO (CuK α radiation = 1.5406 Å). The results were obtained at room temperature in the 2 θ range between 5° and 80°. The lattice constant (a, b, c) and the unit cell volume (V) were refined thru the least square method using FullProf software. To investigate the vibration absorption modes, Fourier-transform infrared (FTIR) spectra were measured via the KBr technique using

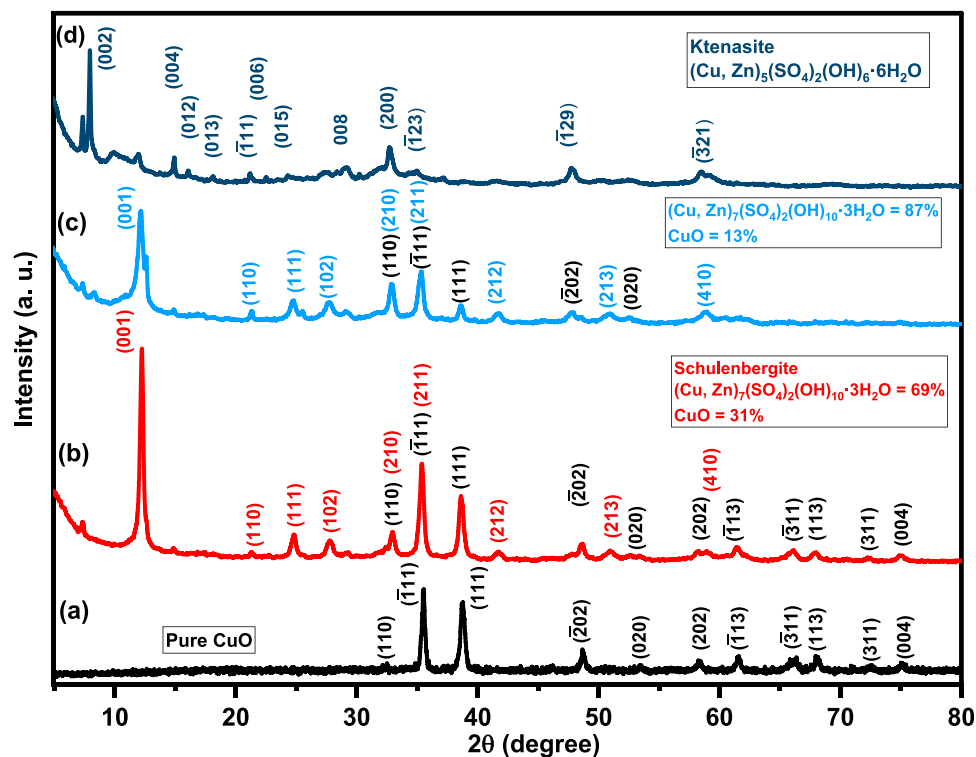
JASCO model 4600 spectrometer. The scanning electron microscope (SEM) and transmission electron microscope (TEM) images were achieved by model Quanta 250 FEG and JEOL JEM-2100, respectively. The energy-dispersive X-ray (EDX) spectroscopy was carried out to examine the elemental composition. The diffuse reflectance analysis of the synthesized powders was carried out by using a double beam spectrophotometer-JASCO (model V-570 UV-Vis-NIR). At room temperature, the ac electrical conductivity, dielectric constant (relative permittivity) and dielectric loss tangent (tan δ) properties were measured using LCR meter (Hitester, model Hioki 3532-50, made in Japan). For electrical measurements, the synthesized powders were converted to pellets form with diameter of 1 cm and thickness of 2.5 mm.

3 Results and discussion

3.1 XRD study

Figure 1 demonstrates the XRD diffraction patterns of pure CuO as well as the prepared powders through the addition of Na₂S with concentration of 0.1, 0.2 and 0.4 mol L⁻¹ to CuO nanoparticles dispersed into Zn(NO₃)₂·6H₂O solution. In case of pure CuO, the XRD peaks located at 2 θ = 32.42°, 35.37°, 38.62°, 48.61°, 52.66°, 58.26°, 61.42°, 66.08°, 67.93°, 72.4° and 74.98° were indexed to (110), (-111), (111), (-202), (020), (202), (-113), (-311), (113) (311) and (004) crystallographic planes of monoclinic CuO structure, Fig. 1a, which in agreement with standard International Centre for Diffraction Data (ICDD, PDF-4+ card file no: 89-2530, space group: C2/c). The X-ray diffraction patterns of the powders produced by the addition of 0.1 and 0.2 mol L⁻¹ Na₂S substance to CuO dispersed into Zn(NO₃)₂·6H₂O solution prove the formation of schulenbergit mineral [(Cu,Zn)₇(SO₄)₂(OH)₁₀·3H₂O] with ratio of 69% (the remainder 31% CuO) and 87% (the remainder 13% CuO), respectively, as shown in Fig. 1b and c. Exactly, The diffraction peaks located at 2 θ = 12.24°, 21.31°, 24.80°, 27.77°, 32.95°, 35.37°, 41.70°, 50.85° and 58.94° were assigned to (001), (110), (111), (102), (210), (211), (212), (213) and (410) crystallographic planes of hexagonal schulenbergit mineral in agreement with the standard data (PDF-4+ card file no: 38-0349, space group: P^{*}, - 3 (147). Whereas, the XRD peaks situated at 2 θ = 32.42°, 35.37°, 38.62°, 48.61°, 52.66°, 58.26°,

Fig. 1 X-ray diffraction patterns of **a** pure CuO, **b** schulenbergite/CuO (69/31%), **c** schulenbergite/CuO (87/13%) and **d** pure ktenasite powders produced by addition of different Na₂S concentrations to CuO–Zn(NO₃)₂·6H₂O solution



61.42°, 66.08°, 67.93°, 72.4° and 74.98° were assigned to (110), ($\bar{1}11$), (111), ($\bar{2}02$), (020), (202), ($\bar{1}13$), ($\bar{3}11$), (113) (311) and (004) crystallographic planes of monoclinic CuO phase (PDF-4+ card file no: 89-2530, space group: C2/c (15)). The ratio of hexagonal schulenbergite mineral to monoclinic CuO which formed due to addition of 0.1 mol L⁻¹ Na₂S was 69–31%, respectively. Whereas, the obtained ratio of hexagonal schulenbergite mineral to monoclinic CuO after addition of 0.2 mol L⁻¹ Na₂S was 87–13%, respectively.

As illustrated in Fig. 1d, the X-ray diffraction pattern of the powder produced by the addition of 0.4 mol L⁻¹ Na₂S substance to CuO dispersed into Zn(NO₃)₂·6H₂O solution confirms the formation of new compound indexed to pure ktenasite mineral [(Cu,Zn)₅(SO₄)₂(OH)₆·6H₂O]. Typically, the XRD peaks recorded at 2θ = 7.64°, 14.90°, 16.07°, 18.09°, 21.18°, 22.50°, 24.30°, 30.21°, 32.72°, 34.94°, 47.75° and 58.52° were ascribed to (002), (004), (012), (013), ($\bar{1}11$), (006), (015), (008), (200), ($\bar{1}23$), ($\bar{1}29$) and ($\bar{3}21$) crystallographic planes of pure ktenasite mineral. The crystallite size and microstrain of schulenbergite/CuO (69/31%), schulenbergite/CuO (87/13%) and pure ktenasite samples were calculated by Williamson–Hall (W–H) method [36–39]:

$$\beta \cos \theta = (K\lambda/D) + 4\epsilon \sin \theta, \quad (1)$$

where β represents the full width at half maximum, θ signifies to peak angle ($2\theta/2$), K is a constant, λ indicates the wavelength of the incident XRD-ray (0.15406 nm), D point to the crystallite size and ϵ represents the microstrain of the samples. As demonstrated in Fig. 2, the plot of $\beta \cos \theta$ against $4\sin \theta$ yields the microstrain from the slope and the crystallite size from the intercept ($D = K\lambda/\text{intercept}$). In case of schulenbergite/CuO (69/31%) sample the crystallite size (D) and the microstrain (ϵ) were estimated to be 36 nm and 0.000025, respectively. For schulenbergite/CuO (87/13%) sample, the crystallite size and the microstrain were valued to be 29 nm and 0.00076, respectively. with respect to pure ktenasite powder, the identified crystallite size and microstrain were 93 nm and 0.003, respectively.

3.2 FTIR vibrational modes

Figure 3 demonstrates the FTIR vibrational absorption modes of the produced powders by addition of 0.1, 0.2 and 0.4 mol L⁻¹ Na₂S to mixture of CuO–Zn(NO₃)₂·6H₂O solution. The FTIR of the synthesized

Fig. 2 Williamson–Hall plot ($\beta\cos\theta$ vs. $4\sin\theta$) of **a** schulenbergite/CuO (69/31%), **b** schulenbergite/CuO (87/13%) and **c** pure ktenasite powders

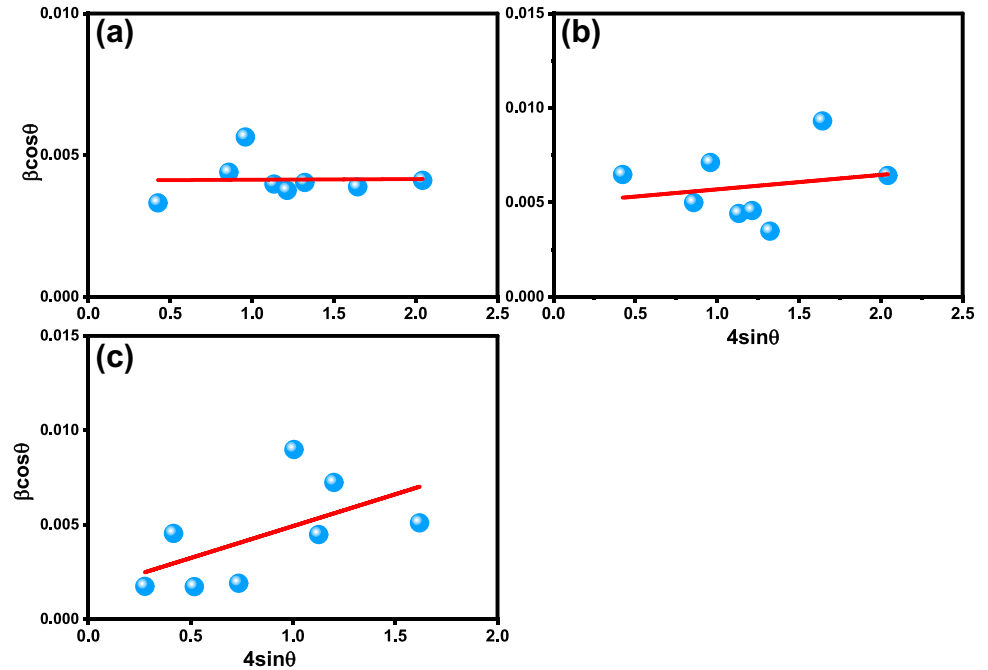
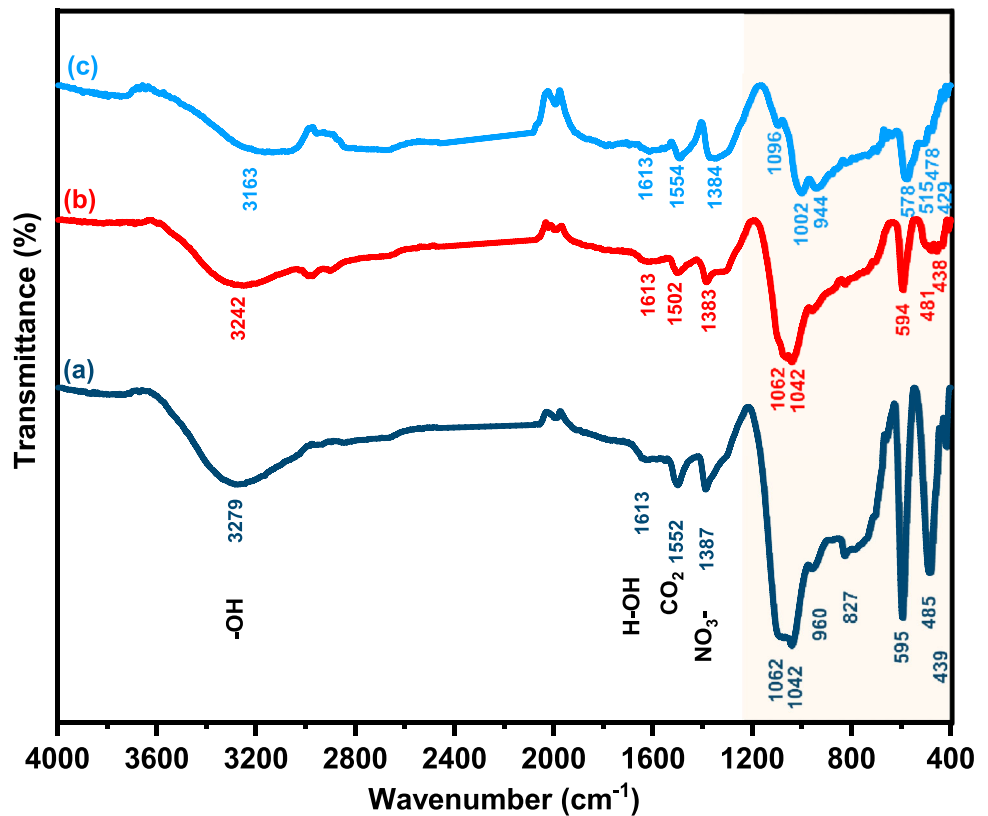


Fig. 3 FTIR vibrational absorption spectra of **a** schulenbergite/CuO (69/31%), **b** schulenbergite/CuO (87/13%) and **c** ktenasite powders produced by addition of different Na_2S concentrations to $\text{CuO-Zn}(\text{NO}_3)_2 \cdot 6\text{H}_2\text{O}$ solution



schulenbergite/CuO mineral (69/31%) shows the presence of eleven vibrational absorption bands positioned at wavenumber of 3279, 1613, 1552, 1387, 1062, 1042, 960, 827, 595, 485 and 439 cm^{-1} , Fig. 3a. In

details, the absorption band located at 3279 cm^{-1} was assigned to the stretching vibration of the O–H groups while the band situated at 1613 cm^{-1} was recognized to H–O–H bend vibration [30–32]. The

two weak absorption bands detected at 1552 and 1387 cm^{-1} can be attributed to the adsorbed CO_2 and/or the residual nitrate group (from starting zinc nitrate material) linked to surface of the synthesized powder, respectively [40, 41]. The absorption bands sited at 1062 and 1042 cm^{-1} and the shoulder band at 960 cm^{-1} were attributed to the vibration of SO_4 group [30–32]. In the low wavenumber region, the various absorption bands which situated at 827, 595, 485 and 439 cm^{-1} can be ascribed to the vibration of $(\text{Cu,Zn})_7$ octahedra of schulenbergite mineral and monoclinic Cu–O bonds vibrations [30–32, 42, 43]. With respect to schulenbergite/CuO mineral (87/13%), Fig. 3b, similar absorption bands to the previous sample were detected, but the intensities of the absorption bands related to CuO component were weak. In case of pure ktenasite sample, Fig. 3c, the FTIR spectrum shows the existence of variable absorption bands situated at 3163, 1613, 1554, 1384, 1096, 1002, 944 and 578, 515, 478 and 429 cm^{-1} [30–32, 40, 41]. The vibration bands centered at 3163, 1613, 1554 and 1384 cm^{-1} were recognized for O–H stretching vibration, H–O–H bend vibration, CO_2 and/or the residual nitrate group vibrations, respectively. The absorption vibration bands within 1100–400 cm^{-1} can be ascribed to SO_4 group and $(\text{Cu,Zn})_5$ octahedral of ktenasite mineral as well as minor Cu–O component which may be present in the sample but lower than the detectable range of the XRD technique.

3.3 Morphological and compositional study: SEM–EDX

Figure 4 shows the scanning electron microscope (SEM) micrographs as well as the parallel 3D view of the synthesized schulenbergite/CuO (69/31%), schulenbergite/CuO (87/13%) and pure ktenasite powders. As illustrated in Fig. 4a, the image of the synthesized schulenbergite/CuO (69/31%) powder displays the presence of little particles have needle and sheets shapes with major particles have cotton-like structure. The SEM micrograph of the schulenbergite/CuO (87/13%) powder exhibits sheets or potato chips structure with different size agglomerated together in large masses. In case of pure ktenasite mineral powder, the particles have cotton or wool shapes. Figure 5 displays the energy dispersive X-ray (EDX) patterns of schulenbergite/CuO (69/31%),

schulenbergite/CuO (87/13%) and pure ktenasite powders. The EDX verify the existence of zinc (Zn), copper (Cu), sulfur (S) and oxygen (O) without existence of any other chemical elements; the EDX technique cannot detect hydrogen (H). The EDX spectra indicated that the sulfur weight% was increased from 6.8 wt% to 10.26 and 12.97 wt% with increasing the concentration of Na_2S from 0.1 to 0.2 and 0.4 mol L^{-1} , respectively. In the same context, the wt% of the zinc element was increased from 18.87 wt% to 25.43 and 42.26 wt% with increasing the concentration of Na_2S from 0.1 to 0.2 and 0.4 mol L^{-1} , respectively. On contrast, the wt% of copper element was decreased from 49.63 wt% to 29.97 and 20.58 wt% with increasing the concentration of Na_2S from 0.1 to 0.2 and 0.4 mol L^{-1} , respectively.

3.4 Transmission electron microscopy

The transmission electron microscope (SEM) images and the corresponding selected area electron diffraction (SAED) patterns of the synthesized schulenbergite/CuO (69/31%), schulenbergite/CuO (87/13%) and pure ktenasite powders were illustrated in Fig. 6. In case of schulenbergite/CuO (69/31%) sample, it can be seen the formation of wrapped threads and nearly sheets particles agglomerated together, Fig. 6a. With respect to schulenbergite/CuO (87/13%) sample, elongated rods overlapped with sheets particles were noticed as shown in Fig. 6b. The TEM image of the pure ktenasite powder, Fig. 6c, displays the presence of elongated particles and cotton-like agglomerated particles. The corresponding SAED patterns of all the synthesized samples obviously show the existence of strong dots-rings (consecutive circles), indicating a high crystalline nature.

3.5 Optical characteristics

The optical properties of the synthesized schulenbergite/CuO (69/31%), schulenbergite/CuO (87/13%) and pure ktenasite powders were studied by diffuse reflectance technique within wavelength of 200–1800 nm as shown in Fig. 7. In the infrared (700–1800 nm) and visible light (400–700 nm) region, the synthesized compositions exhibit a low diffuse

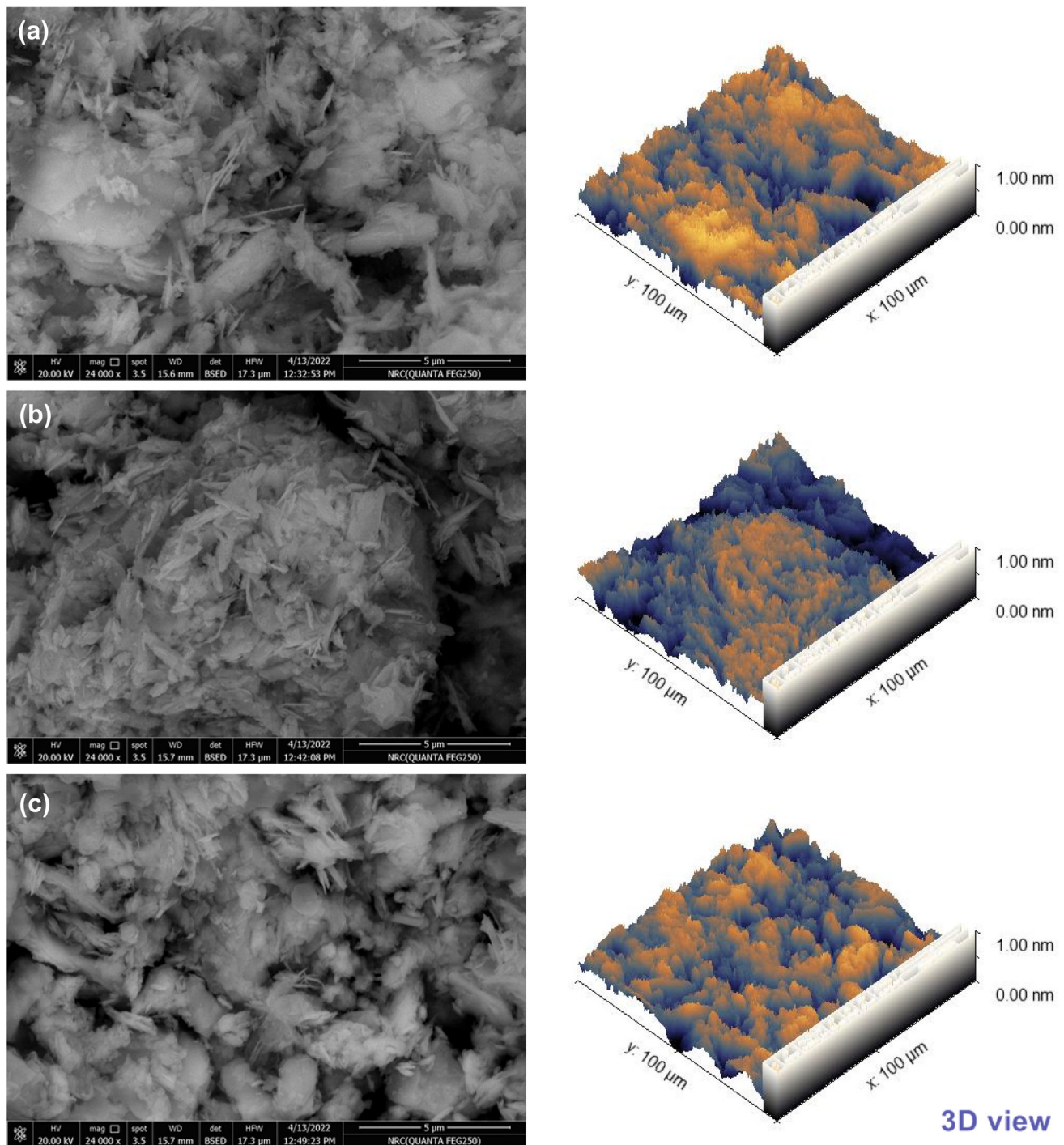


Fig. 4 SEM micrographs and the corresponding 3D view of **a** schulenbergite/CuO (69/31%), **b** schulenbergite/CuO (87/13%) and **c** ktenasite powders produced by addition of different Na₂S concentrations to CuO–Zn(NO₃)₂·6H₂O solution

reflectance intensity (8–18%), signifying to their high absorption abilities. Based on Kubelka–Munk function, plotting of $[F(R)hv]^2$ versus energy (hv) can produce the band gap energies in these compositions [44–47], Fig. 7b. Schulenbergite/CuO (69/31%)

sample reveals a bang gap energy equal to 1.33 eV (932 nm) with additional small band gap at 0.5 eV. Whereas schulenbergite/CuO (87/13%) powder exhibits a band gap energy of 1.63 eV (760 nm) with also additional a small band gap energy at 0.5 eV. In

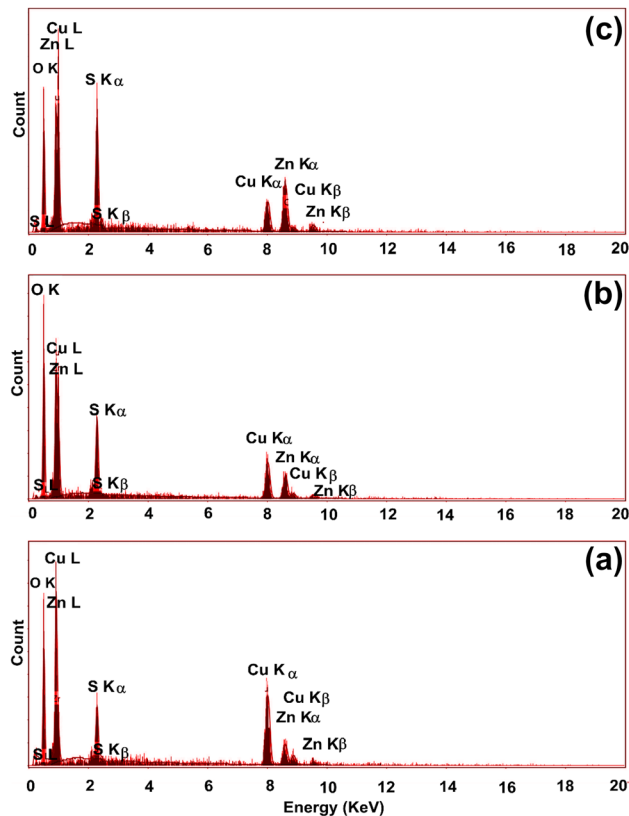


Fig. 5 EDX patterns of **a** schulenbergite/CuO (69/31%), **b** schulenbergite/CuO (87/13%) and **c** ktenasite powders produced by addition of different Na_2S concentrations to $\text{CuO-Zn}(\text{NO}_3)_2 \cdot 6\text{H}_2\text{O}$ solution

case of pure ktenasite composition the bang gap energy was estimated to be 1.3 eV (953 nm) plus small band gap energy of 0.5 eV. The results of the optical characteristics point out that the synthesized compositions have a small band gap energies, signifying to their high absorption ability of longer wavelengths which is an important factor in the photocatalytic applications.

3.6 Relative permittivity and electrical conductivity properties

Figure 8 illustrates the changes of the relative permittivity (dielectric constant) and dissipation factor ($\tan \delta$) with the applied frequency (42 Hz–5 MHz) at room temperature. For all samples, the relative permittivity shows regular decreases with increasing the applied frequency, but at very high frequencies the relative permittivity approximately become constant. At lower frequencies, giant dielectric constant values

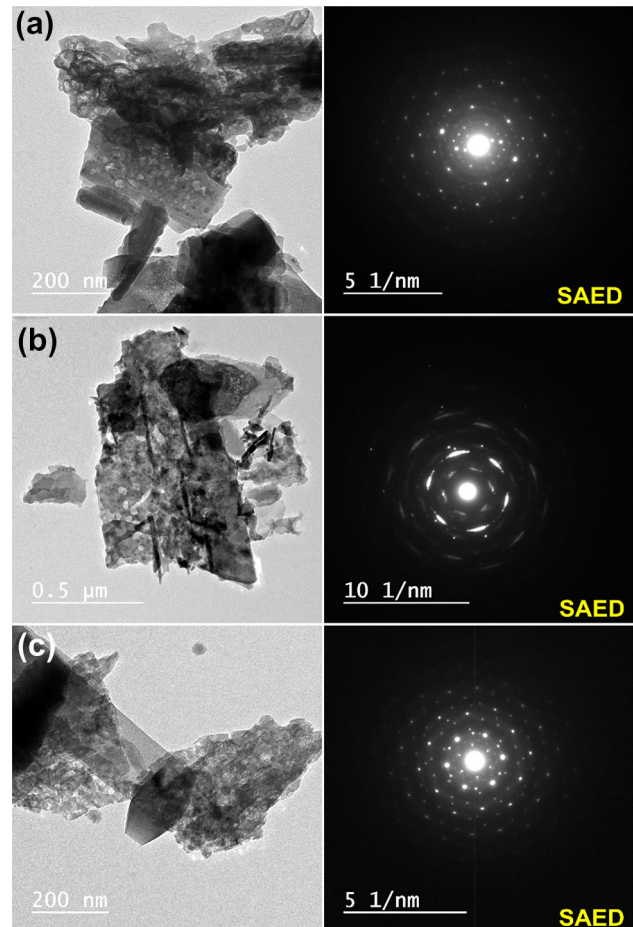


Fig. 6 TEM and the corresponding SAED images of **a** schulenbergite/CuO (69/31%), **b** schulenbergite/CuO (87/13%) and **c** pure ktenasite powders produced by addition of different Na_2S concentrations to $\text{CuO-Zn}(\text{NO}_3)_2 \cdot 6\text{H}_2\text{O}$ solution

was found for pure ktenasite sample with measured value of $\sim 1.3 \times 10^6$ at 42 Hz. For schulenbergite/CuO (87/13%) sample, a large dielectric constant value of ~ 5311 at 42 Hz was found. On contrast, a low relative permittivity value of 56 at 42 Hz was detected for schulenbergite/CuO (69/31%) sample. The dielectric constant values at 42, 100, 250, 500, 1000 and 5000 Hz for all samples were tabulated in Table 1. The dielectric constant behavior of the synthesized samples with frequency are similar to those observed for many metal oxides and can be described by using Maxwell–Wagner model (interfacial polarization) which in agreement with Koop's phenomenological theory [48–53]. Numerous kinds of polarization including ionic polarization, electronic polarization, space charges polarization, molecular orientation, chain relaxation or free counter ions

Fig. 7 **a** Variation of reflectance (%) with wavelength and **b** Kubelka–Munk plot for band gap determination of schulenbergite/CuO (69/31%), schulenbergite/CuO (87/13%) and pure ktenasite samples produced by addition of different Na₂S concentrations to CuO-Zn(NO₃)₂·6H₂O solution

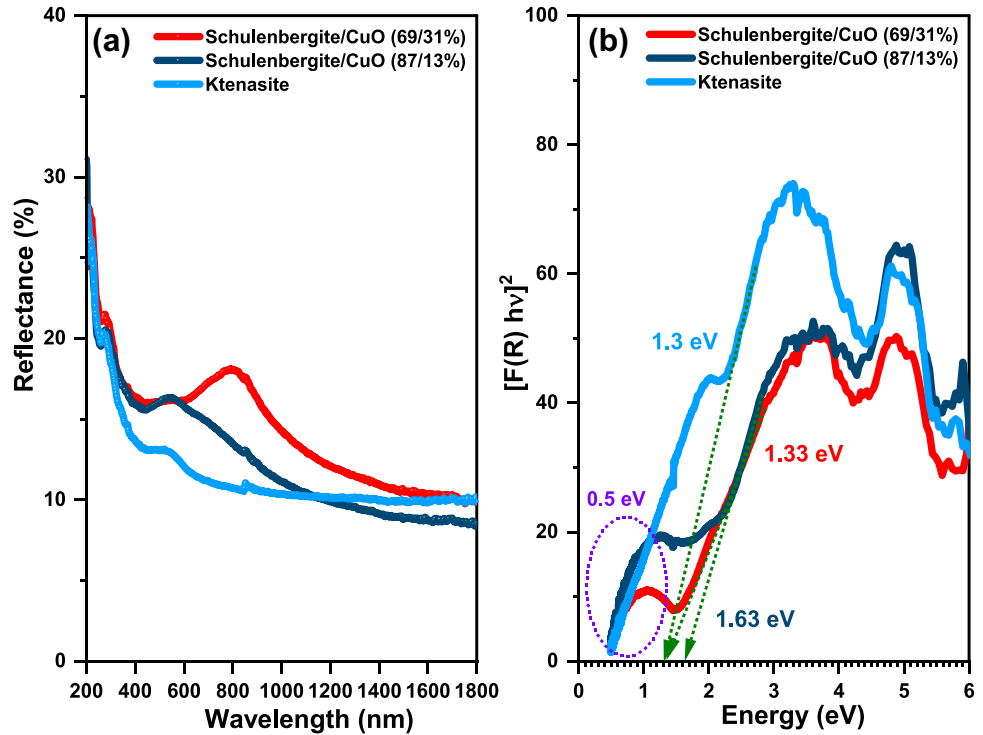
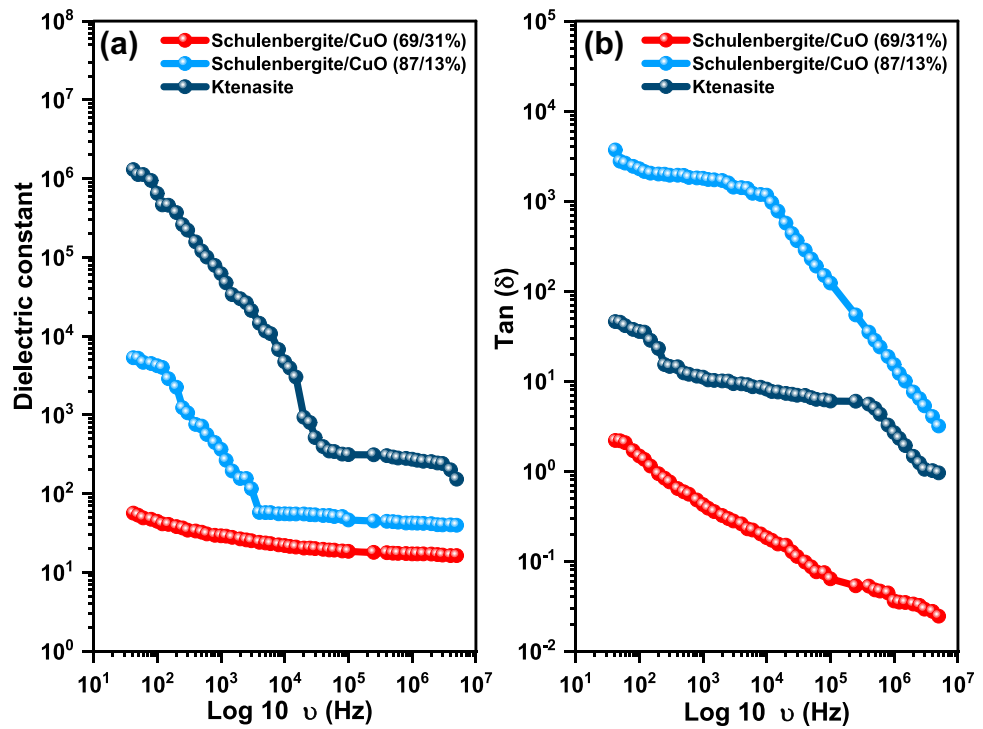


Fig. 8 **a** Variation of dielectric constant with frequency and **b** variation of tan (δ) with frequency of schulenbergite/CuO (69/31%), schulenbergite/CuO (87/13%) and pure ktenasite samples



polarization, electrode or electric double-layer (EDL) polarization can contribute to the relative permittivity (dielectric constant) values [54]. At lower frequencies the space charges polarization is existing, Debye oriented polarization above 10⁴ Hz and

beyond this frequency other polarizations like atomic, ionic and electronic are be existent. Accordingly, at lower frequencies the interfacial polarization or space charges polarization which related to the grain boundaries leading to the large values of the

Table 1 Dielectric constant values at 42, 100, 250, 500, 1000 and 5000 Hz for the synthesized samples

	42 Hz	100 Hz	250 Hz	500 Hz	1000 Hz	5000 Hz
Schulenbergite/CuO(69/31%)	56	44	36	32	29	23
Schulenbergite/CuO(87/13%)	5310	4206	1233	716	364	57
Ktenasite	12,99,824	645,568	259,345	120,359	62,096	11,642

relative permittivity. At small frequencies, the space charges polarization is noticeable owing to the trapped electric charges at the grain boundaries; the grain boundaries act as a barrier against the movement of the charge carriers. The presence of these barriers lead to formation of thin spatial charge layer (sub-grain boundary) in the neighborhood of the grain boundaries. At lower frequencies, the colossal values of the relative permittivity can be clarified in dual routes; in first the grain boundaries or interfaces of compacted particles contains an abundant arrangement of defects. At the grain boundaries, these imperfections lead to the changing of the positive and negative space-charge distributions. When the pellet samples are exposed to an external electric field, the positive and negative space-charges at grain boundaries transfer towards the negative and positive poles of applied electric field, respectively. Meanwhile, a large number of dipole moments are unavoidably created after they have been trapped by defects. As a result, the space-charge polarization at grain boundaries results in the large dielectric constant values for pure ktenasite material. Secondly, the pure ktenasite material may possess a particular surface with great density of disordered ions such as negative ions of numerous sulfur vacancies and positive ions of high number of Cu^{2+} which can act as shallow donors at the grain boundaries. In the system, the integration of the sulfur vacancies and copper gaps may cause the foundation of dipole moments. Numerous of these dipole moments can switch under the effect of the applied electric field. In this case, at the grain boundaries the rotation-direction polarization takes place which finally contribute to the relative permittivity of pure ktenasite sample.

Figure 8b shows the variation of the dielectric loss tangent ($\tan \delta$, dissipation factor) which represents the convert of the electrical energy to heat of the dielectric material. The $\tan \delta$ values were decreased with increasing the applied frequency for all samples. The schulenbergite/CuO (87/13%) sample exhibits the highest value of the dielectric loss factor. Although ktenasite material reveals huge dielectric constant but it

shows a low dielectric loss factor ($\tan \delta$) compared to schulenbergite/CuO(87/13%) sample. The lowest $\tan \delta$ values was achieved for the schulenbergite/CuO (69/31%) sample. In the same context, the performance of the $\tan \delta$ can be explained by using Maxwell–Wagner and Koop’s phenomenological theories [48–53]. At the low frequency, the big value of $\tan(\delta)$ can be ascribed to the large resistivity of grain boundaries which are more effective than the grains. Figure 9 demonstrates the frequency dependence of the ac conductivity of schulenbergite/CuO (69/31%), schulenbergite/CuO (87/13%) and pure ktenasite samples. The schulenbergite/CuO (69/31%) sample shows the lowest ac electrical conductivity. On contrast, schulenbergite/CuO (87/13%) and pure ktenasite samples reveal a high ac electrical conductivity. With increasing the frequency, the enhancements of σ_{ac} can be explained by using Maxwell–Wagner interfacial theory [48–53]. With increasing of the applied frequency, the charge carriers achieve the adequate energies to move over the potential barrier which yields the high progress in the σ_{ac} . On contrast, at small frequencies, the low progress in the σ_{ac} can be attributed to the fewer electric charges that can tunnel over the potential barrier. In this work, the dielectric measurements point out that the pure ktenasite mineral has giant and variable relative permittivity values with low dielectric loss tangent which make ktenasite structure as a promising material for energy capacitive storage applications.

4 Conclusions

In this study, the electrical and dielectric properties of schulenbergite/CuO (69/31%), schulenbergite/CuO (87/13%) and pure ktenasite samples were studied for energy capacitive storage applications. The structural analysis confirmed that the Na_2S concentration has a main role on the schulenbergite $[(\text{Cu,Zn})_7(\text{SO}_4)_2(\text{OH})_{10}\cdot 3\text{H}_2\text{O}]$ and ktenasite $[(\text{Cu,Zn})_5(\text{SO}_4)_2(\text{OH})_6\cdot 6\text{H}_2\text{O}]$ minerals formation. The X-ray diffraction data illustrated that schulenbergite/CuO (69/

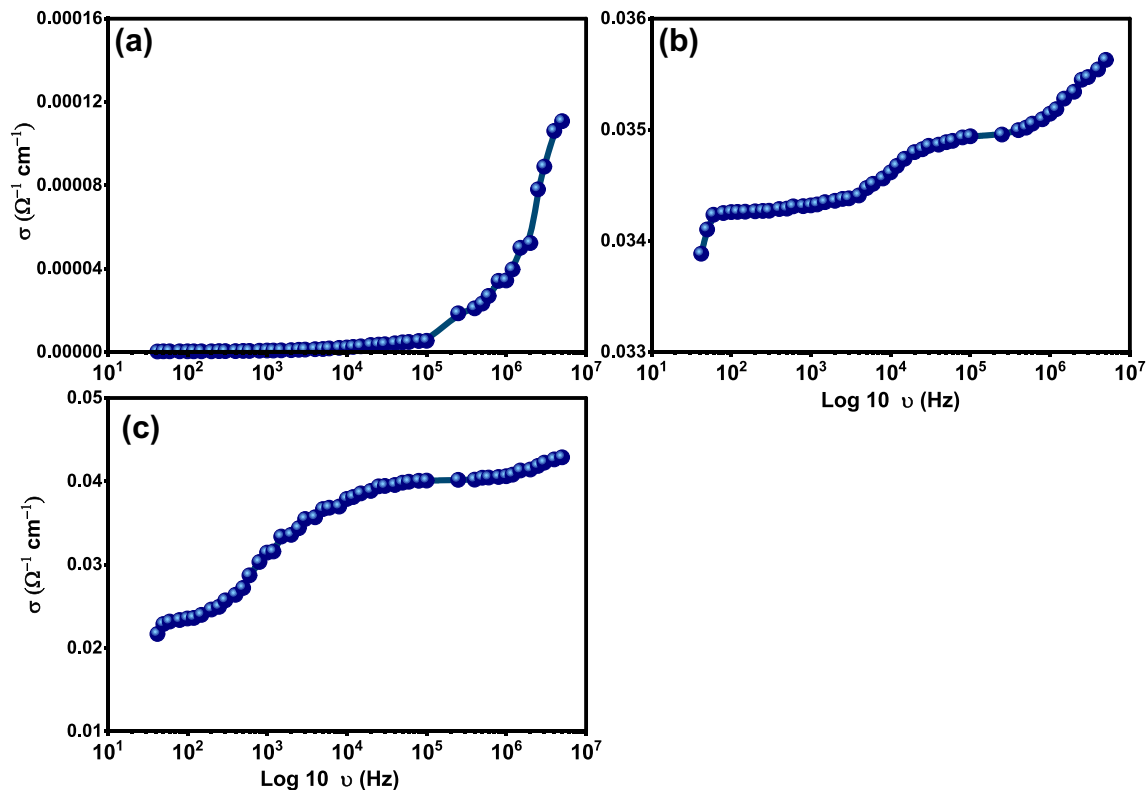


Fig. 9 Shows the changes of the ac electrical conductivity with applied frequency of **a** schulenbergite/CuO (69/31%), **b** schulenbergite/CuO (87/13%) and **c** pure ktenasite samples

31%) and schulenbergite/CuO (87/13%) composites were formed owing to addition of 0.1 and 0.2 mol L⁻¹ Na₂S, respectively. Pure ktenasite mineral was formed after increasing the Na₂S concentration to 0.4 mol L⁻¹. Morphologically, schulenbergite and ktenasite powders reveals mixture grains of needle, sheets and wool shapes. Transmission electron microscopy (TEM) and selected area electron diffraction (SAED) observation show the formation of particles of different shapes with obvious crystalline nature. The results of the dielectric constant verified that ktenasite sample exhibits colossal relative permittivity at lower frequencies with recorded value of $\sim 1.3 \times 10^6$ at frequency of 42 Hz. The giant dielectric constant values of pure ktenasite mineral is suitable for energy capacitive storage applications.

Author contributions

All authors have equal contributions (study conception, design, material preparation, data collection and written of the final manuscript).

Funding

Open access funding provided by The Science, Technology & Innovation Funding Authority (STDF) in cooperation with The Egyptian Knowledge Bank (EKB). The authors have not disclosed any funding.

Data availability

The datasets generated during and/or analyzed during the current study are available from the corresponding author on reasonable request.

Declarations

Conflict of interest The authors declare that they have no known competing financial interests or personal relationships that could have appeared to influence the work reported in this paper.

Open Access This article is licensed under a Creative Commons Attribution 4.0 International License, which permits use, sharing, adaptation, distribution and reproduction in any medium or format, as long as you give appropriate credit to the original author(s) and the source, provide a link to the Creative Commons licence, and indicate if changes were made. The images or other third party material in this article are included in the article's Creative Commons licence, unless indicated otherwise in a credit line to the material. If material is not included in the article's Creative Commons licence and your intended use is not permitted by statutory regulation or exceeds the permitted use, you will need to obtain permission directly from the copyright holder. To view a copy of this licence, visit <http://creativecommons.org/licenses/by/4.0/>.

References

- F.T. Szczypinski, S. Bennett, K.E. Jelfs, *Chem. Sci.* **12**, 830–840 (2021)
- O.M. Yaghi, M. O’Keeffe, N.W. Ockwig, H.K. Chae, M. Eddaoudi, J. Kim, *Nature*. **423**, 705–714 (2003)
- A.A.H. El-Bassuony, H.K. Abdelsalam, *Phys. Scr.* **98**, 055919 (2023)
- A.A.H. El-Bassuony, W.M. Gamal, H.K. Abdelsalam, *Eur. Phys. J. Spec. Top.* (2023). <https://doi.org/10.1140/epjs/s11734-022-00759-4>
- W.M. Gamal, A.A.H. El-Bassuony, R.S. Hafez, H.K. Abdelsalam, *JOM*. **74**, 4898–4908 (2022)
- A.A.H. El-Bassuony, W.M. Gamal, H.K. Abdelsalam, *J. Mater. Sci. Mater. Electron*. **33**, 16219–16235 (2022)
- J. Wei, Z. Sun, W. Luo, Y. Li, A.A. Elzatahry, A.M. Al-Enizi, Y. Deng, D. Zhao, *J. Am. Chem. Soc.* **139**, 1706–1713 (2017)
- J. Amouroux, P. Siffert, J.P. Massué, S. Cavadias, B. Trujillo, K. Hashimoto, P. Rutberg, S. Dresvin, X. Wang, *Prog. Nat. Sci. Mater. Int.* **24**, 295–304 (2014)
- S.P. Bandi, S. Bhatnagar, V.V.K. Venuganti, *Acta Biomater.* **119**, 13–29 (2021)
- C. Wu, K. Wang, M. Batmunkh, A.S.R. Bati, D. Yang, Y. Jiang, Y. Hou, J.G. Shapter, S. Priya, *Nano Energy*. **70**, 104480 (2020)
- J.-M. Rueff, M. Poienar, A. Guesdon, C. Martin, A. Maignan, P.-A. Jaffrès, *J. Solid State Chem.* **236**, 236–245 (2016)
- A. Ali, A. Andriyana, *RSC Adv.* **10**, 16390–16403 (2020)
- P. Kum-onsa, P. Thongbai, B. Putasaeng, T. Yamwong, S. Maensiri, *J. Eur. Ceram. Soc.* **35**, 1441–1447 (2015)
- L. Yuan, L. Li, G. Li, S. Wang, J. Li, D. Lu, W. Han, *Ceram. Int.* **45**, 17705–17714 (2019)
- M.A. Mahdi, S.R. Yousefi, L.S. Jasim, M. Salavati-Niasari, *Int. J. Hydrog. Energy*. **47**, 14319–14330 (2022)
- S.R. Yousefi, M. Ghanbari, O. Amiri, Z. Marzhooseyni, P. Mehdizadeh, M. Hajizadeh-Oghaz, M. Salavati-Niasari, *J. Am. Ceram. Soc.* **104**, 2952–2965 (2021)
- S.R. Yousefi, H.A. Alshamsi, O. Amiri, M. Salavati-Niasari, *J. Mol. Liq.* **337**, 116405 (2021)
- S.R. Yousefi, A. Sobhani, H.A. Alshamsi, M. Salavati-Niasari, *RSC Adv.* **11**, 11500–11512 (2021)
- S.R. Yousefi, O. Amiri, M. Salavati-Niasari, *Ultrason. Sonochem.* **58**, 104619 (2019)
- S.R. Yousefi, D. Ghanbari, M. Salavati-Niasari, M. Hassanspour, *J. Mater. Sci. Mater. Electron*. **27**, 1244–1253 (2016)
- P. Mehdizadeh, M. Jamdar, M.A. Mahdi, W.K. Abdulsahi, L.S. Jasim, S.R. Yousefi, M. Salavati-Niasari, *Arab. J. Chem.* **16**, 104579 (2023)
- S.R. Yousefi, M. Masjedi-Arani, M.S. Morassaei, M. Salavati-Niasari, H. Moayedi, *Int. J. Hydrog. Energy*. **44**, 24005–24016 (2019)
- M.-Y. Tse, X. Wei, C.-M. Wong, L.-B. Huang, K. Lam, J. Dai, J. Hao, *RSC Adv.* **8**, 32972–32978 (2018)
- M.R. Ghazanfari, A. Santhosh, J.C. Vrijmoed, K. Siemensmeyer, B. Peters, S. Dehnen, P. Jerabek, G. Thiele, *RSC Adv.* **12**, 30514–30521 (2022)
- B. Wang, Y. Pu, L. Zhang, Y. Shang, J. Ji, T. Wei, T. Ouyang, S. Zhou, D. Wang, *Ceram. Int.* **48**, 25484–25494 (2022)
- N.T. Taylor, F.H. Davies, S.G. Davies, C.J. Price, S.P. Heplestone, *Adv. Mater.* **31**, 1904746 (2019)
- S. Lunkenheimer, S. Krohns, S.G. Riegg, A. Ebbinghaus, A. Reller, Loid, *Eur. Phys. J. Spec. Topics* **180**, 61–89 (2010)
- Z. Peng, J. Wang, P. Liang, J. Zhu, X. Zhou, X. Chao, Z. Yang, *J. Eur. Ceram. Soc.* **40**, 4010–4015 (2020)
- Y.L. Zheng, X.B. Zhao, Q.H. Zhao, J.C. Li, Q.B. Zhang, *Geomech. Geophys. Geo-energy. Geo-resour.* **6**, 22 (2020)
- P. Elliott, *Acta Cryst. B* **75**, 1069–1075 (2019)
- M. Ohnishi, I. Kusachi, S. Kobayashi, J. Yamakawa, *J. Mineral. Petrol. Sci.* **102**, 233–239 (2007)
- M. Xue, R. Chitrakar, K. Sakane, K. Ooi, S. Kobayashi, M. Ohnishi, A. Doi, *J. Solid State Chem.* **177**, 1624–1630 (2004)
- Z. Delcheva, N. Petrova, T. Stanimirova, *Rev. Bulgar. Geol. Soc.* **81**, 25–27 (2020)
- R.L. Frost, B.J. Reddy, E.C. Keeffe, *Transit. Met. Chem.* **35**, 667–678 (2010)
- A.V. Kasatkin, S.N. Britvin, N.V. Chukanov, R. Škoda, A.A. Agakhanov, D.I. Belakovskiy, *Geol. Ore Depos.* **62**, 599–607 (2020)
- A.K. Bhunia, P.K. Jha, S. Saha, *BioNanoScience* **10**, 917–927 (2020)

37. A.K. Bhunia, S. Saha, *J. Mater. Sci. Mater. Electron.* **32**, 9912–9928 (2021)
38. R. Samui, A.K. Bhunia, S. Saha, *J. Mater. Sci. Mater. Electron.* **34**, 742 (2023)
39. A.K. Bhunia, S. Saha, *BioNanoScience* **10**, 89–105 (2020)
40. A. Gankanda, D.M. Cwiertny, V.H. Grassian, *J. Phys. Chem. C* **120**, 19195–19203 (2016)
41. S.M. Yakout, *Ceram. Int.* **46**, 22504–22512 (2020)
42. M.A. Wahba, T.A. Hameed, W. Sharmoukh, S.M. Yakout, *Opt. Mater.* **127**, 112254 (2022)
43. T.A. Hameed, S.M. Yakout, M.A. Wahba, W. Sharmoukh, *Opt. Mater.* **133**, 113029 (2022)
44. W. Sharmoukh, T.A. Hameed, S.M. Yakout, *J. Alloys Compd.* **925**, 166702 (2022)
45. S.M. Yakout, A.M. Youssef, M.A. Wahba, W. Sharmoukh, A.M. El Sayed, MSh. Khalil, *J. Magn. Magn. Mater.* **561**, 169751 (2022)
46. T.N. Ghosh, S.S. Pradhan, S.K. Sarkar, A.K. Bhunia, *J. Mater. Sci. Mater. Electron.* **32**, 19157–19178 (2021)
47. A.K. Bhunia, T.N. Ghosh, K. Bhunia, S. Saha, *Appl. Phys. A* **129**, 81 (2023)
48. C. Rayssi, S. El.Kossi, J. Dhahri, K. Khirouni, *RSC Adv.* **8**, 17139–17150 (2018)
49. A. Bougoffa, E.M. Benali, A. Benali, M. Bejar, E. Dhahri, M.P.F. Graça, M.A. Valente, G. Otero-Irurueta, B.F.O. Costa, *RSC Adv.* **12**, 6907–6917 (2022)
50. A.M. Youssef, S.M. Yakout, *J. Solid State Chem.* **308**, 122902 (2022)
51. A.M. Youssef, S.M. Yakout, *Mater. Chem. Phys.* **282**, 125978 (2022)
52. A.K. Bhunia, S.S. Pradhan, K. Bhunia, A.K. Pradhan, S. Saha, *J. Mater. Sci. Mater. Electron.* **32**, 22561–22578 (2021)
53. T.N. Ghosh, A.K. Bhunia, S.S. Pradhan, S.K. Sarkar, *J. Mater. Sci. Mater. Electron.* **31**, 15919–15930 (2020)
54. N.K. Chourasia, A. Sharma, V. Acharya, N. Pal, S. Biring, B.N. Pal, *J. Alloys Compd. Vol.* **777**, 1124–1132 (2019)

Publisher's Note Springer Nature remains neutral with regard to jurisdictional claims in published maps and institutional affiliations.